Materials and Design 110 (2016) 18–26

Contents lists available at ScienceDirect

Materials and Design

journal homepage: www.elsevier.com/locate/matdes

TiO_2 anatase intermediary layer acting as template for ZnO pulsed electrodeposition

Tânia Frade [a], Killian Lobato [b], José F.C. Carreira [c], Joana Rodrigues [c], Teresa Monteiro [c], Anabela Gomes [a,*]

[a] Centro de Química e Bioquímica, Faculdade de Ciências, Universidade de Lisboa, 1749-016 Lisboa, Portugal
[b] Instituto Dom Luiz, Faculdade de Ciências, Universidade de Lisboa, 1749-016 Lisboa, Portugal
[c] Departamento de Física e I3N, Universidade de Aveiro, Campus Universitário de Santiago, 3810-193 Aveiro, Portugal

HIGHLIGHTS

- First report on the use of a TiO_2 intermediate layer for the growth n-type ZnO nanorod arrays by pulsed electrodeposition.
- Importantly, films are compared to those grown without a TiO_2 intermediate layer but with the same ZnO seed layer.
- In this case results show that nanorod density increases 3-fold to ~$165\mu m^{-2}$ and nanorod diameter decreases by 50% to ~40nm.
- Results also show that green intra-bandgap photoluminescence emission is suppressed indicating enhanced crystalline quality.

GRAPHICAL ABSTRACT

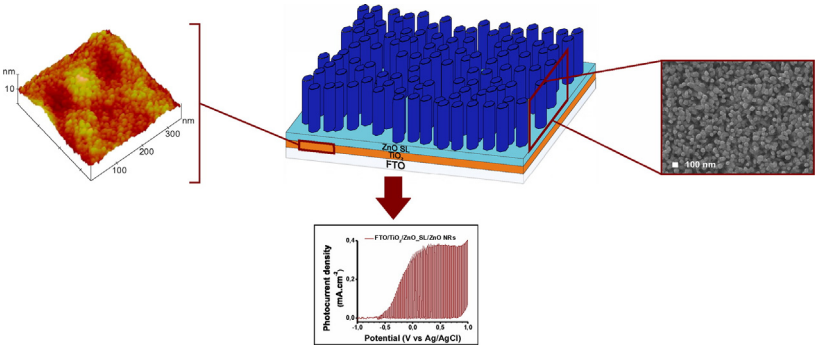

ARTICLE INFO

Article history:
Received 18 May 2016
Received in revised form 16 July 2016
Accepted 25 July 2016
Available online 26 July 2016

Keywords:
Nanostructures
Pulsed electrodeposition
ZnO
TiO_2 intermediate layer
Electron transfer
Photoelectrochemical behaviour

ABSTRACT

Zinc oxide nanorod (ZnO NR) films for photocatalytic and energy conversion applications were synthesized by pulsed electrodeposition. The films were prepared on modified fluorine-doped tin oxide (FTO) glass coated with thin layers of ZnO seeds and porous anatase titanium dioxide (TiO_2). The ZnO seed layers were prepared electrochemically, whilst the TiO_2 layers by spin-coating. Morphological and structural analysis of the films reveal the effect of the TiO_2 intermediate layers on ZnO NRs was to improve vertical alignment, increase spatial density and decrease diameter.

Room temperature photoluminescence (PL) results show that the ZnO NRs exhibit near band edge recombination and deep level emission in the green and red spectral regions. The green emission was almost suppressed for ZnO NRs grown using the TiO_2 intermediate layer followed by two step electrodeposition of ZnO.

The prepared films demonstrated photoelectrochemical behaviour in aqueous electrolytes. Additionally, the ZnO NRs prepared with a TiO_2 intermediate layer demonstrated increased stability to photo-dissolution.

1. Introduction

Zinc oxide (ZnO) is a direct bandgap n-type semiconductor which is transparent in the visible range of the electromagnetic radiation spectrum. Due to its electrical and optical characteristics (e.g. high binding

* Corresponding author.
E-mail address: abmg@fc.ul.pt (A. Gomes).

http://dx.doi.org/10.1016/j.matdes.2016.07.122
0264-1275/

energy of 60 meV at room temperature for the free exciton), it is one of the most promising materials for optical and electronic applications [1,2]. For photovoltaic (PV) applications ZnO has been successfully used in dye-sensitized solar cells [3,4], and recently in perovskite solar cells [5–7].

Different ZnO morphologies, such as nanowires, nanorods, nanosheets, nanobelts and nanotubes can be obtained depending on the growth conditions. Of these morphologies 1D ZnO nanostructures should be the most favourable as electron collecting layers because they combine direct electron transport pathways with large surface areas [8,9]. The 1D ZnO nanostructures can be prepared by a variety of processes, e.g. sputtering [10], chemical vapour deposition (CVD) [11], atomic layer deposition (ALD) [12], metal organic chemical vapour deposition (MOCVD) [13], sol-gel synthesis [14,15], spray pyrolysis [16] and electrodeposition [17,18]. Due to the a) low temperatures involved (<100 °C), b) growth orientation control of ZnO thin films and c) scalability and hence economic viability, electrodeposition has attracted significant attention for the formation of 1D ZnO nanostructures [19,20]. There are several reports on orientation control of ZnO thin films prepared by electrodeposition [8,21]. Previous reports using electrodeposition techniques employed a constant potential/current, and ZnO films with hexagonal single-crystal columns were attained, which is the most typical morphology obtained by electrodeposition [22–24]. However, the application of a constant potential/current has limitations when tuning some features of ZnO films. Pulsed electrodeposition, for example, has the advantage of promoting nucleation, enabling the formation of fine crystals. This is achieved by the opportunity of adjusting pulse parameters independently over a wide range. The result is the additional diffusion of reacting species, which plays an important role during electrodeposition [19,25,26]. Consequently, by controlling pulse parameters, it should be possible to further optimise films to the desired morphologies. For the electrolyte composition, most reports in the literature use dissolved oxygen as the oxidant [27], although electrodeposition of ZnO from nitrate-based electrolytes has also been extensively studied [22,28]. When compared to the use of O_2 [20,29] or H_2O_2 [30], the use of nitrate-based electrolytes has the advantage of reducing the need for convection and the addition of an extra oxidant.

The substrate onto which the electrodeposition occurs is also a fundamental parameter that defines film growth morphology. For PV application the substrate tends to be a transparent conducting oxide (e.g. FTO or ITO). However, this can be modified with intermediate (or buffer) layers to model ZnO film growth [31–34].

Using a TiO_2 thin layer as a template, ZnO electrodeposition in one or two steps, i.e., with or without a ZnO seed-layer, seems to allow for better control of the nucleation step, which is a crucial factor for ZnO vertical growth [35]. To the best of our knowledge, the use of TiO_2 as an intermediate layer for pulsed electrodeposition of ZnO nanorods has never been reported. As such, the influence on morphology, structure, optical and electrical characteristics of this type of intermediate layer was studied for the pulsed electrodeposition of ZnO nanorods.

2. Experimental procedures

2.1. Pulsed electrodeposition of ZnO 1D nanostructures onto different substrates

The substrates onto which the ZnO nanorods were grown were of four types: 1) bare fluorine-doped tin oxide coated glass (Pilkington TEC 15, 12–14 Ω/□); 2) FTO coated with a ZnO seed-layer; 3) FTO coated with a TiO_2 film and 4) a TiO_2 film coated with a seed-layer of ZnO. These modified substrates are hereafter designated as FTO/ZnO_SL, FTO/TiO_2 and FTO/TiO_2/ZnO_SL respectively.

The FTO substrates were cleaned by ultra-sonicating (Elma S30) sequentially for 15 min in liquid neutral soap, acetone and ethanol (95%). In between sonications the electrodes were rinsed in abundant deionised water (18.2 MΩ.cm). The substrates were then dried in nitrogen (N_2) flux.

The TiO_2 layers (ca. 100 nm in thickness) were prepared by spin-coating (500 rpm for 3 s and 2000 rpm for 30 s) using a solution of 0.15 M titanium diisopropoxide bis(acetylacetonate) (75%, Aldrich) in 1-butanol (Aldrich). Upon deposition the samples were then moved into an oven and heated in air at 125 °C for 5 min. Upon cooling to room temperature (RT), the same spin-coating and heating process was repeated twice, however with a more concentrated solution of 0.30 M titanium diisopropoxide bis(acetylacetonate) in 1-butanol. Finally and upon rinsing in deionised water, these were annealed in air at 500 °C for 15 min inside a muffle furnace. The heating rate was 5 °C.min^{-1} whilst cooling to RT occurred naturally within the furnace.

The ZnO seed-layers (<100 nm thickness) were prepared electrochemically by applying −1.3 V vs Ag/AgCl for 30 s on FTO and FTO/TiO_2 modified substrate surfaces, using an aqueous solution of 10 mM $Zn(NO_3)_2 \cdot 6H_2O$ (98.0%, Sigma-Aldrich) and 5 mM KCl (Sigma-Aldrich) prepared with deionised water as electrodeposition bath, solution pH 6.4. The temperature of the solution was maintained at 70 °C. A Gamry R600 potentiostat/galvanostat was used to perform the electrodeposition processes.

Pulsed electrodeposition of ZnO 1D nanostructures was carried out in a single compartment glass cell using as the working electrodes FTO, FTO/ZnO_SL, FTO/TiO_2, and FTO/TiO_2/ZnO_SL. The electrode area in contact with the electrolyte was a square measuring 2.25 cm^2. A graphite foil (9 cm^2 area) was used as counter electrode and Ag/AgCl (saturated KCl) electrode as reference. The working and counter electrodes were placed parallel to each other separated by a distance of 2 cm. The electrolytic baths were the same as used for ZnO seed-layer electrodeposition. ZnO electrodeposits were prepared by applying a potentiostatic square wave for 60 min. Each cycle consisted of 0.25 s at −1.0 V vs Ag/AgCl and 1 s at 0.0 V.

Finally and upon rinsing in deionised water, the as deposited films were annealed in air at 450 °C for 1 h inside a muffle furnace. As before, the heating rate was 5 °C.min^{-1} whilst cooling to RT occurred naturally within the furnace.

Resultant film thickness varied between ca. 500 nm and 800 nm depending on the substrate used.

2.2. Characterization

2.2.1. Voltammetric studies

Cyclic voltammetry was undertaken to understand the effect the four differing substrates have on ZnO film growth.

The electrolyte composition and conditions and electrode setup were identical to those used for pulsed electrodeposition. Voltammograms were acquired by scanning three times between the open-circuit potential (~0.2 V) and −1.3 V vs Ag/AgCl. The scan rate was 10 mV.s^{-1}.

2.2.2. Morphological, structural and optical characterization

The morphology of ZnO 1D nanostructures was investigated by field-emission scanning electron microscopy (FEG-SEM JEOL JSM-7001F).

The surface morphology of the TiO_2 films was imaged by atomic force microscopy (Nanoscope IIIa). Acquisition was in tapping mode at a scan rate of 1.5–1.8 Hz. The tips were etched silicon with a resonance frequency of ~300 kHz (TESP, Bruker).

The structural characterization of the films was carried out by X-ray diffraction (XRD) on a Philips PANalytical PW 3050/60 X'Pert PRO (θ/2θ) equipped with an X'Celerator detector and X'Pert Data Collector (v2.0b) software, using a monochomatic Cu-K_α radiation as the incident beam, operating at 40 kV and 30 mA. XRD patterns were obtained by continuous scanning in the 2θ-range from 20 to 90°. The preferred orientation of the ZnO 1D nanostructures was estimated from the X-ray data according to the methodology developed by Bérubé et al. [36], considering the three Miller indexes of the four usually used to describe the

hexagonal modified ZnO wurtzite structure, where the relative texture coefficient (*RTC*) is calculated by the expression described in Eq. (1).

$$RTC_{(hkl)} = \frac{R_{(hkl)}}{\sum R_{(hkl)}};\ R_{(hkl)} = \frac{I_{s(hkl)}}{I_{p(hkl)}} \quad (1)$$

$I_{s(hkl)}$ and $I_{p(hkl)}$ correspond to the diffraction intensities of the (*hkl*) planes measured for the films and the standard ZnO sample, respectively. In this investigation, (100), (002), and (101) ZnO diffraction maxima were considered.

The optical behaviour of the films was evaluated by measuring their transmission spectra in the 200–800 nm range. These were recorded with a UV–Vis spectrophotometer (Shimadzu UV-2600PC).

RT photoluminescence (PL) measurements were performed using above bandgap excitation with 3.8 eV (325 nm) photons from a continuous waveform (CW) He—Cd laser. The luminescence radiation was dispersed by a Spex 1704 monochromator (1 m, 1200 g.mm^{-1}) and detected by a cooled Hamamatsu R928 photomultiplier.

Raman measurements, also conducted at RT, were performed in a Jobin Yvon HR800 spectrometer (1800 g.mm^{-1} diffraction grating) in a backscattering geometry, using 442 nm wavelength radiation from a CW He—Cd laser and a × 100 magnification lens.

2.2.3. Photoelectrochemical characterization

The photoelectroactivity of the ZnO electrodes was evaluated in an aqueous solution of 0.05 M Na_2SO_3 (96.0%, Quimilabo®) (pH ~ 9.5). The photocurrent and photovoltage responses of the films were measured using a three electrode cell with a graphite bar counter and Ag/AgCl reference electrodes. The working electrode was illuminated through the backside (substrate glass) and quartz window of the three electrode cell. The irradiance source was a UV-enhanced mercury-xenon arc lamp (EmArc 200 W Ushio Lighting-Edge Technologies) housed in a Lot Oriel Apex light source and focused with a lens. The placement of the lens and working electrode were adjusted so as to homogenously illuminate the working electrode active area. The estimated irradiance was ~500 mW.cm^{-2}.

Photovoltammograms were obtained by scanning the applied potential between −1.0 V and 1.0 V vs Ag/AgCl at 2 mV.s^{-1}. To eliminate the effect of the dark current, illumination was chopped at 0.1 Hz. Photocurrent-time curves were also obtained by applying 0.4 V vs Ag/AgCl and chopping the illumination at 0.025 Hz. The acquisition time was 3 min. Given the relatively short duration of these photocurrent measurements, the electrolyte was deaerated with N_2 flux for 15 min beforehand.

The open-circuit photovoltage transients under dark and illuminated conditions were also recorded. The temporal profile was 60 min in the dark, followed by 60 min illuminated and finally 10 min in the dark. The electrolyte here was continuously deaerated with N_2 flux.

3. Results and discussion

Voltammetric studies were performed to better understand the electrodeposition of ZnO on FTO and on the three types of modified substrates. Fig. 1 shows a partial close-up view of the negative sweep of the cyclic voltammograms (CV) recorded for FTO and modified surface substrates in an aqueous solution containing 10 mM $Zn(NO_3)_2$ and

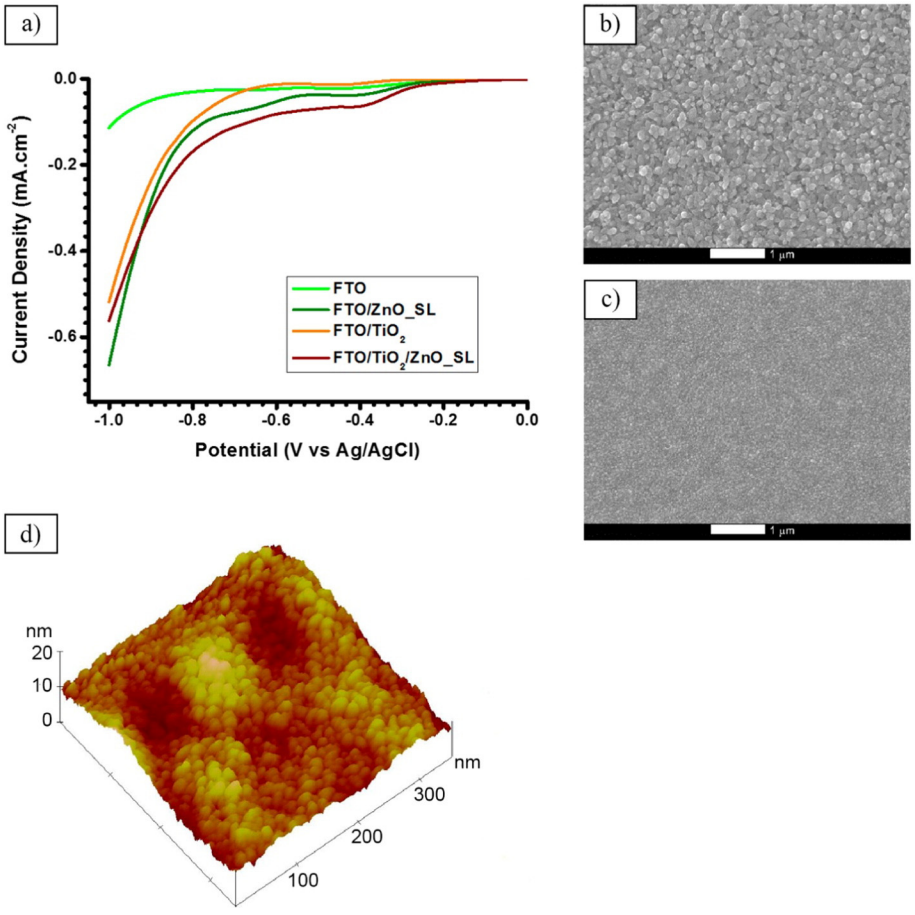

Fig. 1. a) Partial close-up view of the negative sweep of the cyclic voltammograms (first cycle) recorded for FTO and modified substrates in a 10 mM $Zn(NO_3)_2$ and 5 mM KCl aqueous solution containing at 70 °C. Inset: Partial close-up view of the completed CV recorded for TiO_2-coated FTO substrate/electrolyte system. Scan rate at 10 mV.s^{-1}. SEM micrographs of electrodeposited ZnO seed-layers on b) FTO and c) TiO_2-coated FTO substrates. d) 3D-AFM image for TiO_2-coated FTO substrate.

5 mM KCl at 70 °C (the same used for seed layer formation and nanorod growth). At potentials more negative than −0.6 V there is an abrupt increase of the cathodic current density, which is attributed to the reduction of NO_3^- ions. As such, the proposed mechanism of ZnO deposition is the electrochemical reduction NO_3^- ions followed by the chemical formation of $Zn(OH)_2$ and subsequent dehydration to ZnO [28], Eq. (2).

$$Zn^{2+} + NO_3{}^- + 2e^- \rightarrow Zn(OH)_2 + H_2O \quad (2)$$

At −1.0 V vs Ag/AgCl (which is the potential imposed on the cathodic pulse during nanorod growth), the current density follows the sequence FTO < FTO/TiO_2 < FTO/TiO_2/ZnO_SL < FTO/ZnO_SL. This is most probably due to the surface morphology and subsequent areas predisposed for the electrochemical reaction. The resultant seed-layer from electrodeposition on TiO_2 coated FTO is significantly different in morphology to that electrodeposited directly on FTO (Fig. 1b) and c)). The ZnO seed-layer electrodeposited directly on the FTO forms, comparably, larger grains. This is possibly due to the large grain structure of the underlying FTO playing a significant role in the mechanism governing deposition. The ZnO seed-layer electrodeposited on the TiO_2 layer has a significantly finer structure possibly due to the more compact nature of the underlying TiO_2, Fig. 1d).

The cyclic voltammograms (first cycle) recorded for FTO and modified substrates are presented in Fig. S1. The appearance of the two current density crossovers occurs in all the systems, suggesting that ZnO grains were formed. Furthermore, SEM micrographs of the respective films after three CV cycles confirmed their formation (see Fig. S2).

Fig. 2 shows the representative SEM micrographs of electrodeposited ZnO nanorods on FTO and modified substrates. The inclusion of a ZnO seed-layer on the FTO results in an increase in the number of nanorods with a decrease in average diameter when compared to those grown directly on FTO. This effect is enhanced when the ZnO seed-layer is substituted by the TiO_2 intermediate layer. Finally, when the TiO_2 intermediate layer is used in conjunction with the ZnO seed-layer, not only is this effect is further enhanced, but so is the vertical alignment of the nanorods. In summary, the use of a modified FTO/TiO_2/ZnO_SL substrate halves average nanorod diameter (ca. 80 nm to 40 nm) and increases nanorod density by about 7 fold (ca. 25 to 165 μm^{-2}), when compared to the unmodified FTO substrate.

The current transients observed from the pulsed potentiostatic deposition all tended to similar shapes towards the end of deposition (see Fig. S3). The shapes for samples whereby deposition occurred onto modified FTO substrates always showed capacitive anodic and cathodic current spikes with subsequent exponential decays. These can be attributed to the well-known effect of intra-bandgap states in TiO_2 and ZnO acting as electron traps. This is not initially observed for deposition directly on FTO, but becomes evident as ZnO material is deposited. The shapes of the transients towards the end of depositions suggest that the faradaic cathodic charge passed increased with the following order respectively: FTO < FTO/ZnO_SL < FTO/TiO_2 < FTO/TiO_2/ZnO_SL. This suggests more material is deposited in this order. This is supported by the top view SEM micrographs showing a higher nanorod density. Cross-sectional SEM micrographs (see Fig. S4) also show more closely packed and narrower nanorods. However, also evident is that the extra charge does not result in longer nanorods. In fact the tendency is the opposite, decreasing from ca. 800 nm for ZnO_NR layers deposited directly on FTO to 600 nm for ZnO_NR layers deposited on the FTO/TiO_2/ZnO_SL modified substrate. Also estimated from the cross-sectional SEM micrographs were the layer thickness's for spin coated TiO_2 (100 nm) and underlying FTO (300 nm) is also apparent.

The X-ray diffraction (XRD) patterns (Fig. S5), are in line for the hexagonal wurtzite crystalline structure (space group $P6_3mc$) of ZnO (JCPDS 36–1451). The calculated relative texture coefficients for the electrodeposited ZnO nanorods are shown in Table 1 and establish

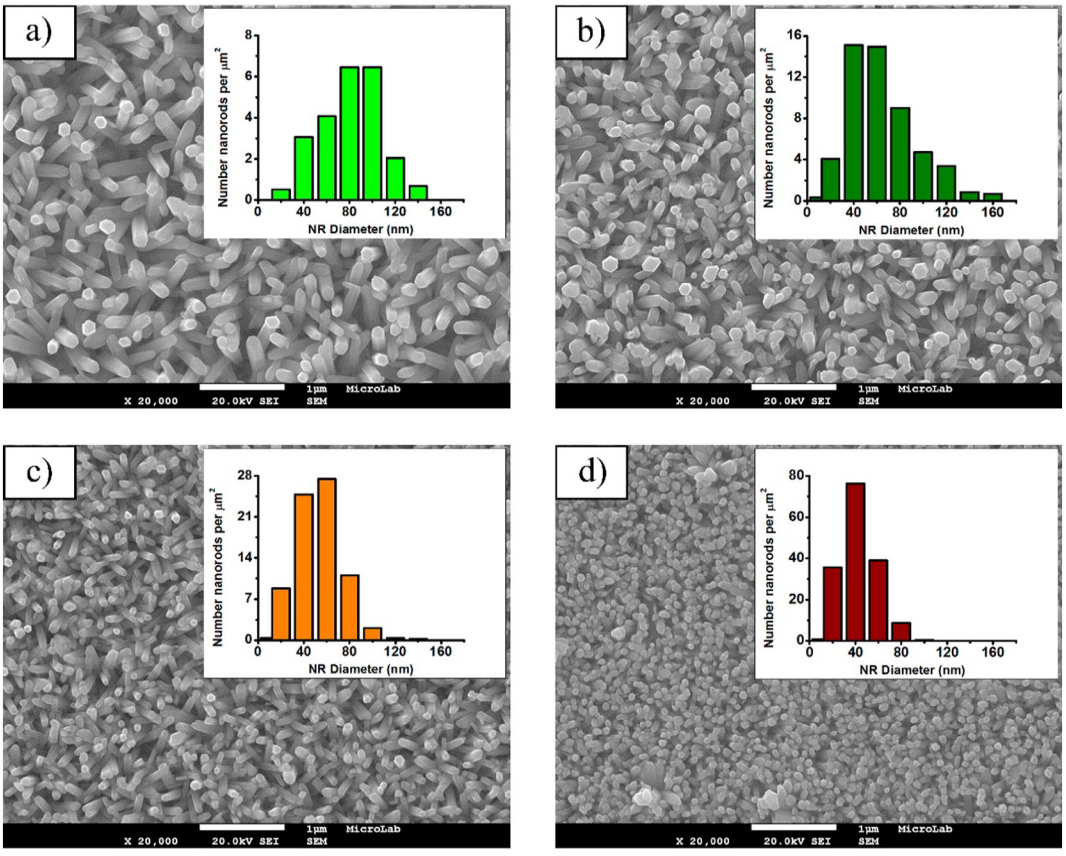

Fig. 2. Representative SEM micrographs of electrodeposited ZnO nanorods on (a) FTO, (b) FTO/ZnO_SL, (c) FTO/TiO_2, and (d) FTO/TiO_2/ZnO_SL substrates. Inset: Histograms of the estimated number of nanorods per area as a function of the diameter.

that the (002) is the preferential orientation. The RTC_{002} is significantly higher, reaching close to 100% for the ZnO nanorods grown on FTO/TiO_2/ZnO_SL substrates. This result is in agreement with what was observed in the SEM micrographs which suggest a more ordered ZnO nanorod growth. Additionally, it was not possible to detect the TiO_2 crystalline structure probably due to its low thickness.

The crystalline quality of the samples was also assessed by Raman spectroscopy. For the ZnO crystalline structure, group theory predicts (for the Γ point of the Brillouin zone) the following optical phonons: $A_1 + E_1 + 2B_1 + 2E_2$. The B_1 modes are silent, while, A_1 and E_1 are polar modes and split into transverse (TO) and longitudinal (LO) optical vibrations [37]. Thus, six active Raman modes are expected. Fig. 3 shows the Raman spectra of the ZnO nanorods grown on FTO and FTO/TiO_2/ZnO_SL templates. For comparison the spectra of glass, FTO and FTO/TiO_2 are also shown. As identified, the Raman spectrum of the glass is responsible for the background observed in all remaining spectra. The FTO spectrum exhibits two main broad resonances located at 561 and 630 cm^{-1} (identified in red), which are in accordance with data reported in the literature [38]. For the FTO/TiO_2 template the typical vibrational modes of TiO_2 in the anatase crystalline phase [39] (identified in blue) were identified. For the ZnO nanorods grown on the FTO/TiO_2/ZnO_SL substrate, apart from the vibrational modes for TiO_2, the expected vibrational frequencies for the hexagonal wurtzite ZnO structure [40] are clearly seen. These modes are identified in black and are indicated in Table 2. These vibrational resonances are the dominant ones for the ZnO nanorods grown on FTO (FTO/ZnO_NR).

Shown in Fig. 4 are Tauc plots obtained from RT absorption spectra of the studied samples. The trend is that the absorption coefficient for photon energies greater that the optical bandgap follows the sequence of FTO/ZnO_NRs, FTO/ZnO_SL/ZnO_NRs, FTO/TiO_2/ZnO_NRs and FTO/TiO_2/ZnO_SL/ZnO_NRs. This increase may be explained by observing that the films respectively present an increasing nanorod number, i.e. there is a greater fraction of absorbing material per unit of volume.

The samples exhibit an absorption onset near 3.2 eV with a steeper gradient for higher energies. This is in fair agreement with the reported ~3.3 eV direct bandgap of ZnO at RT [41]. The optical bandgap was determined via the Tauc method (neglecting band tail effects). For direct bandgap materials a direct transition between the extreme points of the energy-momentum dispersion relation is expected, resulting in the following relationship between the optical absorption coefficient, α, and the incident photon energy $h\nu$ [42],

$$\alpha(h\nu) = A\left(h\nu - E_g\right)^{1/2} \tag{3}$$

where A is a proportionality constant and E_g is the bandgap energy. The results indicate that for ZnO nanorods grown directly on FTO or seed-layer coated FTO the bandgap energy is 3.26 and 3.27 eV, respectively. For ZnO nanorods grown on TiO_2 coated FTO substrates or subsequently coated with a ZnO seed-layer, the bandgap energy is 3.27 and 3.28 eV, respectively. In both cases the estimated values are in agreement for reported values for ZnO [41].

Fig. 5 depicts the normalized RT photoluminescence (PL) results obtained with above bandgap excitation for the ZnO nanorods grown on FTO, FTO/TiO_2 and FTO/TiO_2/ZnO_SL substrates. For comparison the PL spectra of glass, FTO and FTO/TiO_2 obtained with the same excitation energy, are also shown. These last two reveal that the main emission coming from the substrate is responsible for wide unstructured broad bands in the ultraviolet, yellow and red spectral regions observed in all the sample's spectra. The features in the spectra of the ZnO NRs grown on the distinct templates are evidence of optically active defects covering a wide spectral range. The emission peaked at ~3.28 eV (Fig. 5b)), which is an almost mirror image of the absorption, corresponds to the near band edge emission (NBE) of ZnO, typically associated with free exciton recombination and their longitudinal optical phonons (LO) replicas [41,43,44]. However, it should be pointed out that in nanostructured ZnO samples, surface defects could also influence the peak position and spectral shape of the ultraviolet emission [45]. Besides this high energy transition, broad emission bands in the green, orange and red regions were identified in the analysed samples. The main intensity peak was found to occur at ~1.8 eV (red emission peak), with a noticeable high energy shoulder in the green region ~2.5 eV for FTO/ZnO NRs samples. Despite a partial overlap with the Glass/FTO substrate emission, the measured broad luminescence bands in the ZnO nanostructures match those currently reported for bulk, thin films and ZnO nanomaterials [41,43,44,46–48]. The chemical nature of the defects from where the green and red luminescence occurs has generated controversy in the literature. The most common explanation is that these PL bands are due to intrinsic defects. However, in the case of nanostructures, some of the broad emission bands have also been associated to the presence of surface-related defects. An example pointing out to

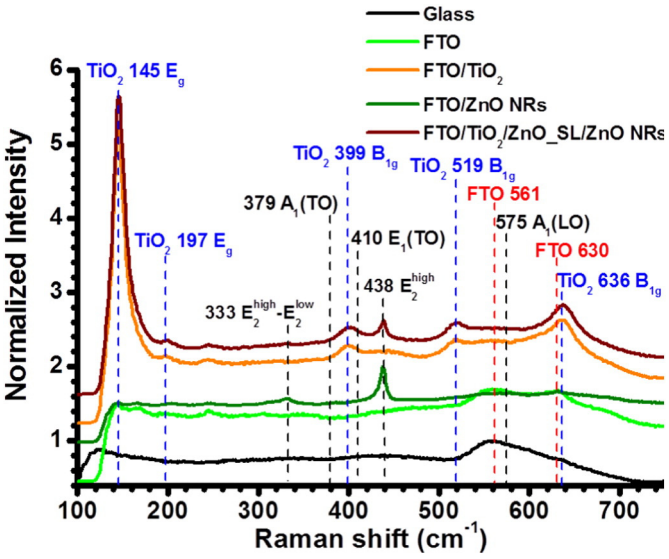

Fig. 3. RT Raman results spectra of the studied samples using a 442 nm wavelength laser line as excitation source. The spectra were obtained in backscattering geometry. ZnO vibrational modes identified in black, FTO substrate in red and TiO_2 in blue. (For interpretation of the references to color in this figure legend, the reader is referred to the web version of this article.)

Table 1
Relative texture coefficient (RTC_{hkl}) of pulsed electrodeposited ZnO nanorods growth on FTO and modified surface substrates.

Sample	RTC_{100} (%)	RTC_{002} (%)	RTC_{101} (%)
FTO/ZnO NRs	8.6	69.9	21.5
FTO/ZnO_SL/ZnO NRs	7.6	78.4	14.0
FTO/TiO_2/ZnO NRs	5.0	76.5	18.5
FTO/TiO_2/ZnO_SL/ZnO NRs	1.0	98.5	0.5

Table 2
Vibrational frequencies observed in this work for ZnO, and in Ref [40], as well, as their symmetry.

Frequency (cm^{-1})		
This work	Ref. [40]	Symmetry
333	333	$E_2^{high} - E_2^{low}$
379	378	$A_1(TO)$
410	410	$E_1(TO)$
438	438	E_2^{high}
575	574	$A_1(LO)$

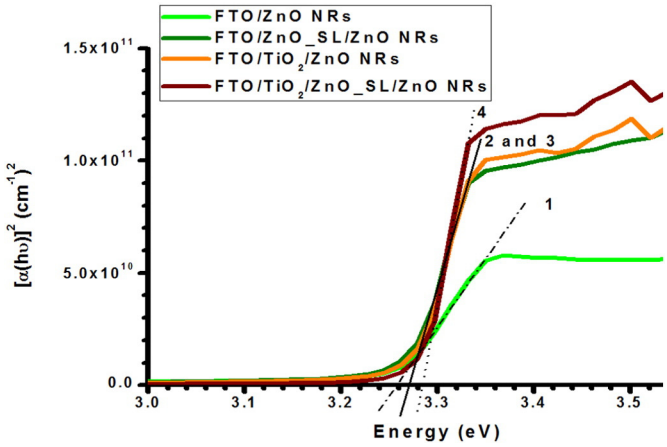

Fig. 4. Tauc plots for electrodeposited ZnO nanorods grown on FTO and modified surface substrates. The line numbered (1) (2) (3) and (4) are the extrapolation lines for FTO/ZnO NRs, FTO/ZnO_SL/ZnO NRs, FTO/TiO_2/ZnO NRs and FTO/TiO_2/ZnO_SL/ZnO NRs respectively.

the presence of such defects is the work reported by Pimentel et al. [49] where the effect of solvent used in ZnO nanorod synthesis was evaluated. In this work, it was observed that the yellow/red emission intensity was strongly sensitive to the laser irradiation time, suggesting that surface mediated processes could be at the origin of the recombination process of the broad visible band.

Typically, the intensity ratio of the NBE/deep level recombination is used as a measure of sample optical quality. Although the ZnO nanorods grown on FTO exhibit a relative increase of the green emission when compared with those grown on FTO/TiO_2/ZnO_SL templates, the intensity ratio of the NBE/deep level recombination is higher for the ZnO nanorods grown directly on FTO, meaning that a higher optical quality is reached for these nanostructures. This conclusion is reinforced by the Raman results, were the ZnO vibrational modes are more intense in FTO/ZnO NR samples than in FTO/TiO_2/ZnO_SL/ZnO NR. In the particular case of the FTO/TiO_2/ZnO_SL/ZnO NR samples, besides the contribution of the FTO substrate, additional contribution of the anatase defects luminescence from the yellow band cannot be discard as TiO_2 is known to emit in this spectral region (under the same excitation conditions) [50,51].

Fig. 6 shows the photovoltammograms for FTO modified substrates in the absence a) and presence b) of grown ZnO nanorods. The obtained photovoltammograms are those expected for nanocrystalline and single crystal electrodes n-type electrodes under reverse bias [52]. There is essentially no dark current flow, except for potentials greater than ~0.7 V (vs Ag/AgCl). This is attributed to the oxidation reaction of SO_3^{2-} species, Eq. (4),

$$SO_3{}^{2-} + 2OH^- \rightarrow SO_4{}^{2-} + H_2O + 2e^- \quad (4)$$

Under illumination three broad regions can be distinguished. At significantly negative potentials, the photocurrent density is zero implying that there is no driving force for efficient electron-hole separation. At intermediate potentials, there is an increase in photocurrent, implying that the driving force for charge separation is dependent on applied bias. At more positive biases, a photocurrent plateau is normally observed, i.e. the driving force is independent of applied bias. Given the morphology of the film, the driving force for electron and hole flow is most likely a mixture of concentration gradient induced diffusion and electric field induced drift.

Observing more closely, the first recognizable fact is that the photoactivity of the films composed by the relatively thin ZnO seed layer or TiO_2 intermediate layer are comparable to those constituted by ZnO nanorods. This can be expected when the absorption spectra of the films are compared (see Fig. S6).

Secondly, films not employing a TiO_2 intermediate layer demonstrate higher photocurrent densities. This appears to be counter to expectation for films that have a more desirable ZnO nanorod morphology (see Fig. 2) and slightly higher absorption coefficients (see Fig. S6).

Thirdly, the films employing a TiO_2 intermediate layer demonstrate onset currents at more negative biases (ca. 250 mV difference). There can be two reasons for this: the first could be due to the relative position of the band edges of the layers, with the TiO_2 layer being more negative than that of the ZnO, considering the reported values of the band edge position of the materials in question [53–55]. The second assumes that the driving force required for efficient charge separation is higher in the ZnO layers than in the TiO_2 layers [56].

Finally, although the films employing ZnO (as a seed layer or nanorod layer) generate greater photocurrent densities, they appear unstable. There is a peak in the photocurrent density with a subsequent decrease.

To further understand the stability of the films, photocurrent transients were recorded by holding the potential at 0.4 V (vs Ag/AgCl), as shown in Fig. 7.

The films employing the TiO_2 intermediate layer have a far more square like and reproducible photocurrent transient. However, a decay in the photocurrent intensity is still observed for films employing both TiO_2 and ZnO layers (either a seed layer or nanorod layer). The decrease in photoactivity may be attributed to the photo-dissolution of ZnO [57–59]. An example of a proposed mechanism is that residual photo-

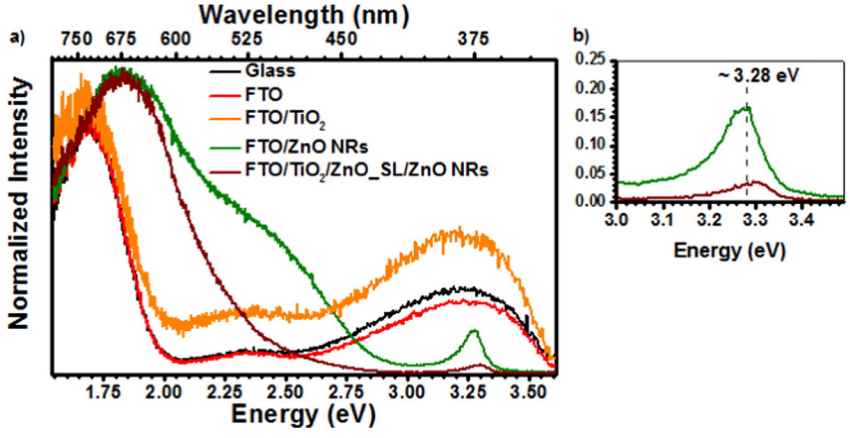

Fig. 5. a) Normalized RT PL spectra of the studied samples with 325 nm wavelength excitation; b) detail of the emission in the UV region.

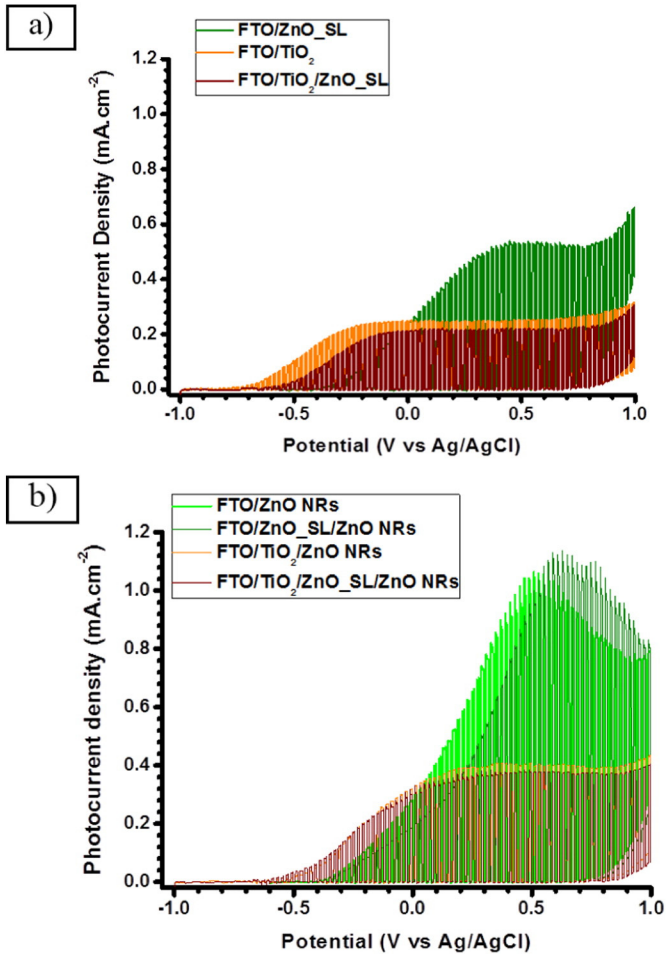

Fig. 6. *j-V* curves of modified surface substrates a) and the corresponding pulsed electrodeposited ZnO nanorods b), obtained in 50 mM Na_2SO_3 aqueous solution (pH ~ 9.5) under illumination chopped at 0.1 Hz. Scan rate of 2 $mV.s^{-1}$.

generated holes on ZnO surfaces attack the Zn—O bonds and dissociate Zn^{2+} from ZnO surface [60],

$$ZnO_{(s)} + h\nu \rightarrow ZnO_{(s)} + h^+ + e^- \quad (5)$$

$$h^+ + e^- \rightarrow h\nu \text{ or } \Delta \qquad \text{recombination} \quad (6)$$

$$ZnO_{(s)} + 2h^+ \rightarrow Zn_{(aq.)}{}^{2+} + \frac{1}{2}O_2 \qquad \text{ZnO photo-dissolution} \quad (7)$$

where $ZnO_{(s)}$ is a solid ZnO film, $h\nu$ is a photon absorbed by the ZnO, h^+ and e^- are the photo-generated hole and electron carriers on the ZnO film surface, and $Zn^{2+}_{(aq.)}$ are Zn^{2+} ions in aqueous solution.

We propose three reasons (but not independent) to explain why films employing the TiO_2 intermediate layer seem to be more chemically stable with time and under illumination.

The first may be due to the crystalline structure of the ZnO. Films with a TiO_2 intermediate layer have a higher RTC_{002} and suppressed some of the green intra-bandgap PL emission, suggesting a lower density of intra-bandgap defect states that can act as hole traps catalysing ZnO photo-dissolution.

The second reason may be due to the light absorption process. The spectrum of the lamp used for the illumination has significant irradiance up to ~5 eV (down to ~250 nm). At these energies the photon penetration depth is approximately 50 to 100 nm, of the order of the thickness's of the TiO_2 intermediate and ZnO seed layers. As illumination was through the substrate side, films employing a TiO_2 intermediate layer have a portion of the absorbable (UV) photons absorbed in the TiO_2 layer and not subsequently in the ZnO. Furthermore, the subsequent layers deposited on the TiO_2 should allow the direct contact between the electrolyte with the TiO_2 layer, promoting hole collection at the electrolyte interface and hence the photocurrent generation, without the deleterious effects of the presence of holes at the ZnO surface.

The third reason may be due to the band alignment of the individual layers. If the TiO_2 bands are more negative than the ZnO bands, then photogenerated electrons in the ZnO layer would be unable to be collected and hence contribute to the photocurrent because of the barrier created by the more negative conduction band edge of the TiO_2 layer. In essence photogenerated electron-hole pairs in the ZnO layer would recombine, preventing the holes from participating in the photodissolution of the ZnO.

The greater photocurrent densities observed for the films employing the ZnO layers without the intermediate TiO_2 layer may be due to more efficient electron-hole pair separation. In this case, there is no TiO_2 layer depriving the ZnO of absorbable photons with the consequence that electron-hole pair generation occurs within the ZnO. The morphologies of the ZnO seed and nanorod layers (see Figs. 1 and 5) suggest a greater surface|electrolyte interface area which is where minority (hole) carrier collection occurs. Also, minority carrier diffusion lengths in anatase TiO_2 are normally reported to be significantly smaller than ZnO [61,62]. It is therefore feasible that a greater fraction of electron-hole pair generation occurs in regions whose distance is smaller than the minority carrier diffusion length resulting in higher internal quantum efficiencies and hence greater photocurrent densities.

Photovoltage transients (shown in Fig. 8) are as expected for n-type semiconductors, with a negative photopotential occurring upon illumination. To a first approximation the photopotential measured is indicative of conduction band edge energy, whereby equilibrium is reached when the Fermi level resides close to the conduction band edge.

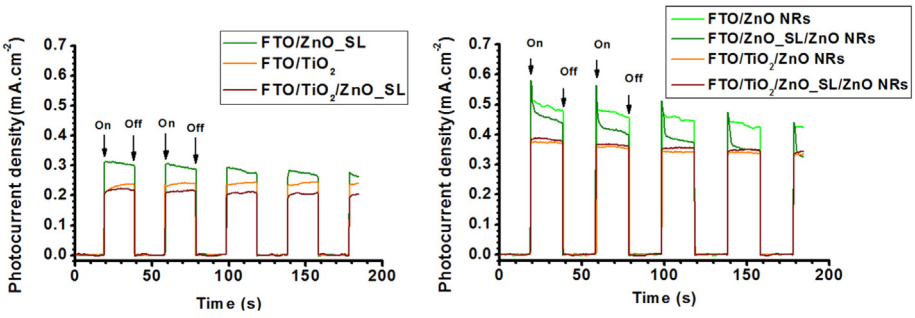

Fig. 7. Photocurrent transients of FTO modified surface substrates and the corresponding pulsed electrodeposited ZnO nanorods, obtained in 50 mM Na_2SO_3 aqueous solution (pH ~ 9.5) under illumination chopped at 0.025 Hz of frequency, at 0.4 V vs Ag/AgCl of applied potential.

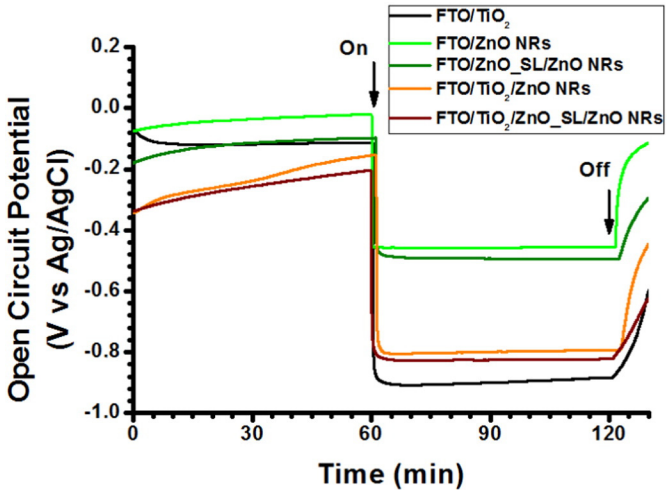

Fig. 8. E_{oc} transients of TiO_2-coated FTO substrate and ZnO nanorods grown on FTO and modified surface substrates.

However, if recombination kinetics are not slow, then a smaller than expected shift in photopotential occurs. There is generally an ~300 mV difference in the potential obtained for films employing a TiO_2 layer when compared to those that do not. This is in line with the observed photocurrent onset potential shift, suggesting that either the band edges are more negative or electron-hole pair recombination is less pronounced in films employing a TiO_2 intermediate layer.

4. Conclusions

Pulsed electrodeposition was successfully applied in the preparation of ZnO nanorods. SEM images and XRD results reveal misoriented vertically aligned ZnO nanorods with improved orientation when a TiO_2 intermediate layer was applied as a template. These also demonstrated a decrease in nanorod diameter and an increase in the number of nanorods per unit of area. Raman results confirmed the hexagonal wurtzite structure of the ZnO nanorods. Additionally for samples containing TiO_2, the vibrational modes on the anatase structure were identified.

The RT PL analyses reveal the presence of the NBE recombination and deep level emission in both FTO/ZnO NR and FTO/TiO_2/ZnO_SL/ZnO NR samples. The intensity ratio of the NBE emission/deep level emission is higher in the FTO/ZnO NR samples indicating higher optical quality of these samples. It should be emphasized that the green emission is almost suppressed in samples with TiO_2 intermediate layer. The optical bandgap estimated from the absorption spectra indicated a value around 3.27 eV. This value is in line with the reported values in the literature for ZnO.

Photoelectrochemical measurements confirmed the n-type photoactivity behaviour of the films. However, all demonstrated instability (to a more or lesser degree) under illumination possibly due to photo-dissolution. Further studies are underway to determine if the stability and photoactivity of the films is altered when illumination is performed through the electrolyte side, whereby light absorption should preferentially occur in the ZnO layers.

For application in solid state devices such as solar cells, the morphology of the films is encouraging as an n-type selective contact with a high surface area and oriented structure.

Acknowledgments

The authors acknowledge financial support from FCT: UID/MULTI/00612/2013, RECI-II/FIS-NAN/0183/2012 (FCOMP-01-0124-FEDER-027494). J. Rodrigues and T. Frade thanks FCT for their respective PhD grants SFRH/BD/76300/2011 and SFRH/BD/84669/2012. The authors are grateful to Dr. A. Viana for the assistance with AFM measurements and Dr. O. Monteiro is gratefully acknowledged for the availability to the UV–Vis spectrophotometer.

Appendix A. Supplementary data

Supplementary data to this article can be found online at http://dx.doi.org/10.1016/j.matdes.2016.07.122.

References

[1] C. Klingshirn, ZnO: material, physics and applications, ChemPhysChem 8 (2007) 782–803.
[2] S. Xu, Z.L. Zhang, One-dimensional ZnO nanostructures: solution growth and functional properties, Nano Res. 4 (2011) 1013–1098.
[3] A. Wagner, A. Behrends, A. Waag, A. Bakin, Two step deposition method with a high growth rate for ZnO nanowire arrays and its application in photovoltaics, Thin Solid Films 520 (2012) 4637–4641.
[4] V.-M. Guérin, J. Rathousky, T. Pauporté, Electrochemical design of ZnO hierarchical structures for dye-sensitized solar cell, Sol. Energy Mater. Sol. Cells 102 (2012) 8–14.
[5] D.-Y. Son, K.-H. Bae, H.-S. Kim, N.-G. Park, Effects of seed layer on growth of ZnO nanorod and performance of perovskite solar cell, J. Phys. Chem. C 119 (2015) 10321–10328.
[6] D.-Y. Son, J.-H. Im, H.-S. Kim, N.-G. Park, 11% efficient perovskite solar cell based on ZnO nanorods: an effective charge collection system, J. Phys. Chem. C 118 (2014) 16567–16573.
[7] J. Zhang, P. Barboux, T. Pauporté, Electrochemical design of nanostructured ZnO charge carrier layers for efficient solid-state perovskite-sensitized solar cells, Adv. Energy Mater. 4 (2014) 1400932.
[8] C. Lévy-Clément, R. Tena-Zaera, M.A. Ryan, A. Katty, G. Hodes, CdSe-sensitized p-CuSCN/nanowire n-ZnO heterojunctions, Adv. Mater. 17 (2005) 1512–1515.
[9] C.V. Manzano, D. Alegre, O. Caballero-Calero, B. Alén, M.S. Martín-González, Structural and optical properties of sol-gel derived nanocrystalline Fe-doped ZnO, J. Appl. Phys. 110 (2011) (043538–043538-8).
[10] S. Eisermann, A. Kronenberger, M. Dietrich, S. Petznick, A. Laufer, A. Polity, B.K. Meyer, Hydrogen and nitrogen incorporation in ZnO thin films grown by radio-frequency (RF) sputtering, Thin Solid Films 518 (2009) 1099–1102.
[11] K.-S. Kim, H.W. Kim, Synthesis of ZnO nanorod on bare Si substrate using metal organic chemical vapor deposition, Physica B 328 (2003) 368–371.
[12] J.M. Huang, C.S. Ku, H.Y. Lee, C.M. Lin, S.Y. Chen, Growth of high-quality epitaxial ZnO films on (10 − 10) sapphire by atomic layer deposition with flow-rate interruption method, Surf. Coat. Technol. 231 (2013) 323–327.
[13] A. Rivera, J. Zeller, A. Sood, M. Anwar, A comparison of ZnO nanowires and nanorods grown using MOCVD and hydrothermal processes, J. Electron. Mater. 42 (2013) 894–900.
[14] L. Znaidi, Sol–gel-deposited ZnO thin films: a review, Mater. Sci. Eng. B 174 (2010) 18–30.
[15] V. Kumar, N. Singh, R.M. Mehra, A. Kapoor, L.P. Purohit, H.C. Swart, Role of film thickness on the properties of ZnO thin films grown by sol-gel method, Thin Solid Films 539 (2013) 161–165.
[16] P. Nunes, B. Fernandes, E. Fortunato, P. Vilarinho, R. Martins, Performances presented by zinc oxide thin films deposited by spray pyrolysis, Thin Solid Films 337 (1999) 176–179.
[17] B.N. Illy, A.C. Cruickshank, S. Schumann, R. Da Campo, T.S. Jones, S. Heutz, M.A. McLachlan, D.W. McComb, D.J. Riley, M.P. Ryan, Electrodeposition of ZnO layers for photovoltaic applications: controlling film thickness and orientation, J. Mater. Chem. 21 (2011) 12949–12957.
[18] T. Pauporté, E. Jouanno, F. Pellé, B. Viana, P. Aschehoug, Key growth parameters for the electrodeposition of ZnO films with an intense UV-light emission at room temperature, J. Phys. Chem. C 113 (2009) 10422–10431.
[19] C. Dunkel, F. Lüttich, H. Graaf, T. Oekermann, M. Wark, Investigation of the pulsed electrochemical deposition of ZnO, Electrochim. Acta 80 (2012) 60–67.
[20] S. Peulon, D. Lincot, Cathodic electrodeposition from aqueous solution of dense or open-structured zinc oxide films, Adv. Mater. 8 (1996) 166–170.
[21] M. Izaki, T. Omi, Characterization of transparent zinc oxide films prepared by electrochemical reaction, J. Electrochem. Soc. 144 (1997) 1949–1952.
[22] M.Z. Khajavi, D.J. Blackwood, G. Cabanero, R. Tena-Zaera, New insight into growth mechanism of ZnO nanowires electrodeposited from nitrate-based solutions, Electrochim. Acta 69 (2012) 181–189.
[23] R. Tena-Zaera, J. Elias, G. Wang, C. Lévy-Clément, Role of chloride ions on electrochemical deposition of ZnO nanowire arrays from O_2 reduction, J. Phys. Chem. C 111 (2007) 16706–16711.
[24] D. Siopa, A. Gomes, Nucleation and growth of ZnO nanorod arrays onto flexible substrates, J. Electrochem. Soc. 160 (2013) D476–D484.
[25] K. Nomura, N. Shibata, M. Maeda, Orientation control of zinc oxide films by pulsed current electrolysis, J. Cryst. Growth 235 (2002) 224–228.
[26] N.P. Klochko, G.S. Khrypunov, Y.O. Myagchenko, E.E. Melnychuk, V.R. Kopach, E.S. Klepikova, V.M. Lyubov, A.V. Kopach, Controlled growth of one-dimensional zinc oxide nanostructures in the pulsed electrodeposition mode, Semiconductors 46 (2012) 825–831.
[27] R. Tena-Zaera, J. Elias, C. Lévy-Clément, I. Mora-Seró, Y. Luo, J. Bisquert, Electrodeposition and impedance spectroscopy characterization of ZnO nanowire arrays, Phys. Status Solidi A 205 (2008) 2345–2350.

[28] M. Wadowska, T. Frade, D. Siopa, K. Lobato, A. Gomes, ZnO nanostructured films electrodeposited at room temperature, ECS Electrochem. Lett. 2 (2013) D40–D42.
[29] J. Elias, R. Tena-Zaera, C. Lévy-Clément, Effect of the chemical nature of the anions on the electrodeposition of ZnO nanowire arrays, J. Phys. Chem. C 112 (2008) 5736–5741.
[30] T. Pauporté, D. Lincot, Hydrogen peroxide oxygen precursor for zinc oxide electrodeposition I. Deposition in perchlorate medium, J. Electrochem. Soc. 148 (2001) C310–C314.
[31] J. Elias, R. Tena-Zaera, C. Lévy-Clément, Electrodeposition of ZnO nanowires with controlled dimensions for photovoltaic applications: role of buffer layer, Thin Solid Films 515 (2007) 8553–8557.
[32] J. Lang, X. Li, J. Yang, Q. Han, Y. Yan, M. Gao, S. Yang, The effect of ZnO buffer layer on structural and optical properties of ZnO nanorods, Cryst. Res. Technol. 46 (2011) 691–696.
[33] S. Sanchez, R. Salazar, C. Lévy-Clément, V. Ivanova, ZnO buffer layers and nanowires electrodeposition for extremely thin absorber solar cells, ECS Trans. 33 (2011) 183–190.
[34] T. Frade, M.E. Melo Jorge, B. Fernández, R. Pereiro, A. Gomes, A possible growth mechanism for ZnO-TiO_2 composite nanostructured films prepared by electrodeposition, J. Electrochem. Soc. 161 (2014) D125–D133.
[35] A.-F. Kanta, A. Schrijnemakers, A. Decroly, Electrochemical characterisations of ZnO nanowires for dye-sensitised solar cells, Mater. Des. 95 (2016) 481–485.
[36] L.P. Bérubé, G. L'Espérance, A quantitative method of determining the degree of texture of zinc electrodeposits, J. Electrochem. Soc. 136 (1989) 2314–2315.
[37] C.A. Arguello, D.L. Rousseau, S.P.S. Porto, First-order Raman effect in wurtzite-type crystals, Phys. Rev. 181 (1969) 1351–1363.
[38] M. Berruet, C.J. Pereyra, G.H. Mhlongo, M.S. Dhlamini, K.T. Hillie, M. Vázquez, R.E. Marotti, Optical and structural properties of nanostructured ZnO thin films deposited onto FTO/glass substrate by a solution-based technique, Opt. Mater. 35 (2013) 2721–2727.
[39] W. Ma, Z. Lu, M. Zhang, Investigation of structural transformations in nanophase titanium dioxide by Raman spectroscopy, Appl. Phys. A Mater. Sci. Process. 66 (1998) 621–627.
[40] R. Cuscó, E. Alarcón-Lladó, J. Ibáñez, L. Artús, J. Jiménez, B. Wang, M.J. Callahan, Temperature dependence of Raman scattering in ZnO, Phys. Rev. B 75 (2007) 165202–165211.
[41] Ü. Özgür, Y.I. Alivov, C. Liu, A. Teke, M.A. Reshchikov, S. Doğan, V. Avrutin, S.-J. Cho, H. Morkoç, A comprehensive review of ZnO materials and devices, J. Appl. Phys. 98 (2005) (041301–041301-103).
[42] J.I. Pankove, Optical Processes in Semiconductors, first ed. Dover Publications Inc., New Jersey, 1971.
[43] B.K. Meyer, H. Alves, D.M. Hofmann, W. Kriegseis, D. Forster, F. Bertram, J. Christen, A. Hoffmann, M. Straßburg, M. Dworzak, U. Haboeck, A.V. Rodina, Bound exciton and donor–acceptor pair recombinations in ZnO, Phys. Status Solidi B 241 (2004) 231–260.
[44] T. Monteiro, A.J. Neves, M.C. Carmo, M.J. Soares, M. Peres, J. Wang, E. Alves, E. Rita, U. Wahl, Near-band-edge slow luminescence in nominally undoped bulk ZnO, J. Appl. Phys. 98 (2005) (013502–013502-6).
[45] A.B. Djurišić, Y.H. Leung, Optical properties of ZnO nanostructures, Small 2 (2006) 944–961.
[46] M. Peres, S. Magalhães, M.R. Soares, M.J. Soares, L. Rino, E. Alves, K. Lorenz, M.R. Correia, A.C. Lourenço, T. Monteiro, Disorder induced violet/blue luminescence in rf-deposited ZnO films, Phys. Status Solidi C 10 (2013) 662–666.
[47] J. Rodrigues, M. Peres, M.R.N. Soares, A.J.S. Fernandes, N. Ferreira, M. Ferro, A.J. Neves, T. Monteiro, F. Costa, ZnO Nano/microstructures grown by laser assisted flow deposition, J. Nano Res. 18-19 (2012) 129–137.
[48] M.A. Reshchikov, H. Morkoç, B. Nemeth, J. Nause, J. Xie, B. Hertog, A. Osinsky, Luminescence properties of defects in ZnO, Physica B 401-402 (2007) 358–361.
[49] A. Pimentel, J. Rodrigues, P. Duarte, D. Nunes, F.M. Costa, T. Monteiro, R. Martins, E. Fortunato, Effect of solvents on ZnO nanostructures synthesized by solvothermal method assisted by microwave radiation: a photocatalytic study, J. Mater. Sci. 50 (2015) 5777–5787.
[50] H. Tang, H. Berger, P.E. Schmid, F. Lévy, G. Burri, Photoluminescence in TiO_2 anatase single crystals, Solid State Commun. 87 (1993) 847–850.
[51] H. Tang, H. Berger, P.E. Schmid, F. Lévy, Optical properties of anatase (TiO_2), Solid State Commun. 92 (1994) 267–271.
[52] T. Berger, D. Monllor-Satoca, M. Jankulovska, T. Lana-Villarreal, R. Gómez, The electrochemistry of nanostructured titanium dioxide electrodes, ChemPhysChem 13 (2012) 2824–2875.
[53] J. Li, N. Wu, Semiconductor-based photocatalysts and photoelectrochemical cells for solar fuel generation: a review, Catal. Sci. Technol. 5 (2015) 1360–1384.
[54] V. Stevanović, S. Lany, D.S. Ginley, W. Tumas, A. Zunger, Assessing capability of semiconductors to split water using ionization potentials and electron affinities only, Phys. Chem. Chem. Phys. 16 (2014) 3706–3714.
[55] Y. Xu, M.A.A. Schoonen, The absolute energy positions of conduction and valence bands of selected semiconducting minerals, Am. Mineral. 85 (2000) 543–556.
[56] R. Beranek, (photo)electrochemical methods for the determination of the band edge positions of TiO_2-based nanomaterials, Adv. Phys. Chem. (2011), 786759 (20 pp.).
[57] P. Spathis, I. Poulios, The corrosion and photocorrosion of zinc and zinc oxide coatings, Corros. Sci. 37 (1995) 673–680.
[58] B. Neppolian, H.C. Choi, S. Sakthivel, B. Arabindoo, V. Murugesan, Solar/UV-induced photocatalytic degradation of three commercial textile dyes, J. Hazard. Mater. 89 (2002) 303–317.
[59] S. Lathasree, A. Nageswara Rao, B. SivaSankar, V. Sadasivam, K. Rengaraj, Heterogeneous photocatalytic mineralisation of phenols in aqueous solutions, J. Mol. Catal. A Chem. 223 (2004) 101–105.
[60] J. Han, W. Qiu, W. Gao, Potential dissolution and photo-dissolution of ZnO thin films, J. Hazard. Mater. 178 (2010) 115–122.
[61] L. Chernyak, E. Flitsiyan, M. Shatkhin, Z. Dashevsky, Studies of electron trapping in ZnO semiconductor, ECS Trans. 28 (2010) 3–11.
[62] T. Luttrell, S. Halpegamage, J. Tao, A. Kramer, E. Sutter, M. Batzill, Why is anatase a better photocatalyst than rutile? Sci. Rep. 4 (2014) 4043.